IMPROVED LABORATORY TRANSITION PROBABILITIES FOR Hf II AND HAFNIUM ABUNDANCES IN THE SUN AND 10 METAL-POOR STARS

(short title: Hf Transition Probabilities and Abundances)

J. E. Lawler, E. A. Den Hartog, Z. E. Labby

Department of Physics, University of Wisconsin, Madison, WI 53706;

jelawler@wisc.edu, eadenhar@wisc.edu, zelabby@wisc.edu

C. Sneden

Department of Astronomy and McDonald Observatory, University of Texas, Austin, TX 78712; chris@verdi.as.utexas.edu

J. J. Cowan

Homer L. Dodge Department of Physics and Astronomy, University of Oklahoma, Norman, OK 73019; cowan@nhn.ou.edu

and I. I. Ivans

The Observatories of the Carnegie Institution of Washington, 813 Santa Barbara St., Pasadena, CA 91101 & Princeton University Observatory, Peyton Hall, Princeton, NJ 08544; iii@ociw.edu

ABSTRACT

Radiative lifetimes from laser-induced fluorescence measurements, accurate to $\sim \pm 5\%$, are reported for 41 odd-parity levels of Hf II. The lifetimes are combined with branching fractions measured using Fourier transform spectrometry to determine transition probabilities for 150 lines of Hf II. Approximately half of these new transition probabilities overlap with recent independent measurements using a similar approach. The two sets of measurements are found to be in good agreement for measurements in common. Our new laboratory data are applied to refine the hafnium photospheric solar abundance and to determine hafnium abundances in 10 metal-poor giant stars with enhanced r-process abundances. For the Sun we derive $\log \varepsilon(Hf) = 0.88 \pm 0.08$ from four lines; the uncertainty is dominated by the weakness of the lines and their blending by other spectral features. Within the uncertainties of our analysis, the r-processrich stars possess constant Hf/La and Hf/Eu abundance ratios, $\log \varepsilon(\text{Hf/La}) =$ $-0.13 \pm 0.02 \ (\sigma = 0.06)$ and $\log \varepsilon (Hf/Eu) = +0.04 \pm 0.02 \ (\sigma = 0.06)$. The observed average stellar abundance ratio of Hf/Eu and La/Eu is larger than previous estimates of the solar system r-process-only value, suggesting a somewhat larger contribution from the r-process to the production of Hf and La. The newly determined Hf values could be employed as part of the chronometer pair, Th/Hf, to determine radioactive stellar ages.

Subject headings: atomic data — Sun: abundances — stars: (HD 74462, HD 115444, HD122956, HD 165195, HD 175305, HD 186478, HD 221170, BD +17°3248, CS 22892-052, CS 31082-001), nucleosynthesis, abundances — Galaxy: evolution

1. INTRODUCTION

Studies of heavy element nucleosynthesis have advanced rapidly in recent years due to enormous improvements in observational capabilities and significant improvements in basic atomic spectroscopic data. High-resolution, high signalto-noise (S/N) spectra on a variety of targets from very large ground-based telescopes and the Hubble Space Telescope are now available. Observations of old metal-poor Galactic halo stars are central to many of these studies because such stars provide a fossil record of the chemical make-up of our Galaxy when it, and the Universe, were very young (e.g., Gratton & Sneden 1994; McWilliam et al. 1995; Cowan et al. 1995; Sneden et al. 1996, Ryan et al. 1996, Cayrel et al. 2004). Abundance determinations of heavy n(eutron)-capture elements in very metal-poor stars are being improved and are steadily yielding new insights on the roles of the r(apid)- and s(low)-processes in the initial burst of Galactic nucleosynthesis (e.g. Simmerer et al. 2004, Ivans et al. 2006, Cowan & Sneden 2006). Recent theoretical and observational advances have been made in metalpoor nucleocosmochronometry studies. The detection of a second radioactive element, U, in the spectra of a halo star provides an important constraint on age determinations using Th (Cayrel et al. 2001). The results of these ongoing studies are reshaping our understanding of the chemical evolution of the Galaxy.

This paper reports new results for Hf. The choice of a stable reference element for nucleocosmochronometry is a crucial part of an age determination. It is essential that the radioactive element, Th (Z = 90) or U (Z = 92), and stable reference element(s) were synthesized in the same event. Confidence that the radioactive element and reference element have the same origin increases if the elements have a similar high Z. Accurate, multiple line abundance determinations are difficult for the heaviest elements (Z \sim 90), thus there is some compromise required in the choice of reference element. We propose that Hf (Z = 72) has good potential as a reference element in nucleocosmochronometry. Improved laboratory data, especially atomic transition probabilities, are essential for using Hf as a reference element in nucleocosmochronometry.

The new laboratory measurements reported in § 2 (radiative lifetimes) and § 3 (branching fractions and transition probabilities) of this paper were completed shortly before we learned of an overlapping study by Lundqvist et al. (2006). The partial overlap of the two sets of measurements provides an opportunity to assess systematic uncertainties in modern atomic transition probability determinations based on combining radiative lifetimes from laser induced fluorescence measurements with branching fractions from Fourier transform spectrometry. The good agreement that we find in the comparison of the overlapping measurements provides reassurance that estimates of systematic uncertainties in modern transition probability measurements are reliable.

We apply the new laboratory data to solar and stellar Hf abundances in \S 4. After discussing Hf II line selection, in \S 4.2 we refine earlier determinations of the Solar photospheric hafnium abundance, and \S 4.3 we determine the abundance of hafnium in 10 metal-poor giant stars with enhanced r-process abundances, finding essentially constant Hf/La and Hf/Eu abundance ratios.

These abundances are discussed in \S 5 in the context of r-process nucleosynthesis.

2. RADIATIVE LIFETIME MEASUREMENTS

Radiative lifetimes of 41 odd-parity levels of Hf II have been measured using time-resolved laser-induced fluorescence (LIF) on an atom/ion beam. Only an overview of the experimental method is given here, since the apparatus and technique have been described in many previous publications on other species. The reader is referred to recent work in Eu I, II, and III (Den Hartog et al. 2002) for a more detailed description.

A hollow cathode discharge sputter source is used to produce a slow ($\sim 5 \times 10^4$ cm/s), weakly collimated beam of Hf atoms and ions. A pulsed argon discharge, operating at ~ 0.4 torr with 10 μ s duration, 10 Å pulses, is used to sputter the hafnium foil which lines the hollow cathode. The hollow cathode is closed on one end except for a 1 mm hole, through which the hafnium atoms and ions flow into a low pressure (10^{-4} torr) scattering chamber. This beam is intersected at right angles by a nitrogen laser-pumped dye laser beam 1 cm below the cathode bottom. The laser is tunable over the range 3610 to 7200 Å using a wide array of commercially available dyes. This range is extended down to 2050 Å with the use of frequency doubling crystals. The laser is pulsed at ~ 30 Hz repetition rate with a ~ 3 ns pulse duration, and has a ~ 0.2 cm⁻¹ bandwidth. The laser is used to selectively excite the level to be studied, eliminating the possibility of cascade radiation from higher-lying levels.

Fluorescence is collected in a direction mutually orthogonal to the laser and atomic/ionic beams using a pair of fused-silica lenses that form an f/1 optical system, and detected with a RCA 1P28A photomultiplier tube (PMT). Optical filters, either broadband colored glass filters or narrowband multi-layer dielectric filters, can be inserted between the two lenses to cut down on scattered laser light and to block cascade radiation from lower levels. The signal from the PMT is recorded and averaged over 640 shots using a Tektronix SCD1000 digitizer. Data collection begins after the laser pulse has terminated to make deconvolution of the laser excitation unnecessary. Data are recorded with the laser tuned on and off the excitation transition. The decay rate is extracted from the background-subtracted fluorescence trace by performing a linear least-square fit to a single exponential. This is repeated 5 times to determine the lifetime of the level. The lifetime is measured twice for each level, using a different excitation transition whenever possible. This redundancy helps ensure that the transitions are identified correctly in the experiment, classified correctly, and are free from blends.

The lifetimes reported here have an uncertainty of $\pm 5\%$, except for the shortest lifetimes (<4 ns) for which the uncertainties are ± 0.2 ns. These uncertainties are primarily systematic, not statistical. The possible systematic errors in our measurements must be well understood and controlled in order to achieve this level of uncertainty. They include limits of the electronic bandwidth, cascade fluorescence, Zeeman quantum beats and atomic motion flight-out-of-view effects, among others. The dominant systematic error depends on the lifetime.

For example the bandwidth limits, linearity, and overall fidelity of the electronic detection system results in the increasing fractional uncertainty below 4 ns and a lower limit of ~2 ns for our system. These systematic effects are discussed in detail in earlier publications, (See, for example, Den Hartog et al. 1999; 2002) and will not be discussed further here. As a means of verifying that the measurements are within the stated uncertainties, we perform periodic end-to-end tests of the experiment by measuring a set of well-known lifetimes. These cross-checks include lifetimes of Be I (Weiss 1995), Be II (Yan et al. 1998) and Fe II (Guo et al. 1992; Biémont et al. 1991), covering the range from 1.8–8.8 ns. An Ar I lifetime is measured at 27.85 ns (Volz & Schmoranzer 1998). He I lifetimes are measured in the range 95 – 220 ns (Kono & Hattori 1984).

The results of our lifetime measurements of 41 odd-parity levels of Hf II are presented in Table 1. Energy levels are from the tabulation by Moore (1971). Air wavelengths are calculated from the energy levels using the standard index of air (Edlén 1953). The uncertainty of the lifetimes is the larger of $\pm 5\%$ or ± 0.2 ns.

Also presented in Table 1 is a comparison of our results with those of Lundqvist et al (2006), which are the only other LIF lifetime measurements. Of the 41 measurements, our results overlap for 17 of the 18 radiative lifetimes they report. We see generally good agreement with their results for short lifetimes <5 ns, but their results are slightly, 5-15%, longer than ours for lifetimes in the 10-35 ns range. In the middle of the hafnium data taking we remeasured the Ar I cross check which Volz and Schmoranzer (1998) measured to be 27.85 ns. We reproduced this lifetime within 1%, giving us confidence that we understand the systematics in the 20 to 30 ns lifetime range. This small discordance between our (UW group) measurements and those by the Lund University group of Lundqvist et al. is not serious. The worst disagreement is only 15%, which is only slightly beyond our combined uncertainties. Including all 17 lifetimes for which we overlap, we see a mean difference of +4.5% in the sense of (τ_{Lund} – τ_{UW})/ τ_{UW} and a similar root-mean-squared difference of 7.3% between our sets of measurements. We further discuss this point in the next section.

3. BRANCHING FRACTIONS AND ATOMIC TRANSITION PROBABILITIES

We primarily used spectra from the 1.0 meter FTS at the National Solar Observatory (NSO) for this project on Hf II. A few supplemental measurements on some deep UV lines were recorded in our Univ. of Wisconsin lab using a 1.0 m Acton spectrometer system with a photodiode array and a small pre-monochromator. The 1.0 meter FTS is our preferred instrument for many reasons. It has the large etendue of all interferometric spectrometers, a limit of resolution as small as 0.01 cm⁻¹, wavenumber accuracy to 1 part in 10⁸, broad spectral coverage from the UV to IR, and the capability of recording a million point spectrum in 10 minutes (Brault 1976). All instruments of this type are insensitive to any small drift in source intensity since an interferogram is a simultaneous measurement of all spectral lines.

The energy level structure of Hf II is relatively simple compared to the nearby rare earth elements. The low even-parity levels belong to the ground $5d6s^2$ configuration, the $5d^26s$ configuration starting at $3645~\rm cm^{-1}$, and the $5d^3$ configuration starting at $18,898~\rm cm^1$. Both levels, including the ground $a^2D_{3/2}$ level, of the $5d6s^2$ configuration are known. Only the high-lying 2S level of the $5d^26s$ configuration is unknown, the other 15 levels are known. The $5d^3$ configuration is also nearly complete, except for the higher of the two 2D terms. The absence of unknown low-lying even-parity levels simplified our search for all possible branches from the odd-parity upper levels of this study.

The known low-lying odd-parity configurations of Hf II include the 5d6s6p configuration starting at $28,069 \text{ cm}^{-1}$, and the $5d^26p$ configuration starting at $42,518 \text{ cm}^{-1}$. A parametric study of Hf II by Wyart & Blaise (1990) did reveal two new levels of these odd-parity configurations with energies above $60,000 \text{ cm}^{-1}$, but described the $6s^26p$ configuration as "unrecognizable" due to mixing.

We considered recording new data on Hf II, but found that existing FTS data in the electronic archives of the National Solar Observatory were more than adequate for our project. In order to make our branching fraction measurements as complete as possible, we worked on the 13 spectra listed in Table 2. A co-author and collaborators recorded some of these Hf spectra listed in Table 2 during observing runs in the 1984 period while working on Hf I (Duquette et al. 1986). The other spectra from 1987 listed in Table 2 were recorded by Earl Worden as a guest observer. All 13 spectra were recorded on custom, water-cooled HCD lamps with either Ar or Ne as the buffer gas. A sufficient range of discharge currents was used to check the strongest Hf II lines to lowlying levels for optical depth errors. These potential errors were identified and eliminated by comparing the high- and low-current HCD spectra. Weaker lines are not susceptible to optical depth errors but are more susceptible to error from blending with buffer gas lines and Hf I lines. Buffer gas lines, Hf I lines, and Hf II lines all have a different dependence on discharge current. Furthermore, the ratio of Hf I line intensities to Hf II line intensities is dependent on buffer gas. The comparison of Hf-Ar spectra over a range of currents and the comparison of the Hf-Ne spectrum with Hf-Ar spectra were used in eliminating potential errors from line blends.

The establishment of an accurate relative radiometric calibration or efficiency is critical to a branching fraction experiment. As indicated in Table 2, we depended primarily on the Ar I and Ar II line technique. This calibration technique captures the wavelength-dependent response of detectors, spectrometer optics, lamp windows, and any other components in the light path or any reflections which contribute to the detected signal (such as due to light reflecting off the back of the hollow cathode). The technique is based on a comparison of well-known branching ratios for sets of Ar I and Ar II lines widely separated in wavelength, to the intensities measured for the same lines. Sets of Ar I and Ar II lines have been established for this purpose in the range of 4300 to 35000 cm⁻¹

¹The NSO archives are available at http://nsokp.nso.edu/dataarch.html

(23256 to 2857 Å) by Adams & Whaling (1981), Danzmann & Kock (1982), Hashiguchi & Hasikuni (1985), and Whaling et al. (1993).

Tungsten (W) filament standard lamps are particularly useful near the Si detector cutoff in the 9,000 to 10,000 cm⁻¹ range (11,111 to 10,000 Å) where the FTS sensitivity is changing rapidly as a function of wave number, and near the dip in sensitivity at 12,500 cm⁻¹ (8000 Å) from the aluminum coated optics. Tungsten lamps are not bright enough to be useful for FTS calibrations in the UV region, and UV branches dominate the decay of all the Hf II levels in this study. In general one must be careful when using continuum lamps to calibrate the FTS over wide spectral ranges, because the "ghost" of a continuum is a continuum. The highest current spectrum (see #6 of Table 2) that has redundant Ar line and W lamp calibrations, was very valuable in measurements of weak visible and near IR lines.

Branching fractions were completed for all odd-parity Hf II levels that do not have deep UV branches beyond the limit of our FTS spectra. This list includes all odd-parity levels below $40,000~\mathrm{cm^{-1}}$, except the $\mathrm{y^2F_{5/2}}$ at $38578~\mathrm{cm^{-1}}$, and a few odd-parity levels above 40,000 cm⁻¹. Some of the levels, specifically the high z⁴G levels and the y²D_{3/2} level, have deep UV branches on the FTS spectra but beyond the limit of the Ar line calibration. The deep UV branches from these levels were measured using the 1.0 m Acton spectrometer system with a photodiode array and pre-monochromator as described by Den Hartog et al. (2005). The radiometric response of the Acton spectrometer system in the deep UV was determined using an Ar mini-arc lamp. Our Ar mini-arc lamp was calibrated at NIST and operated without a window (see Bridges & Ott 1977; Klose, Bridges, & Ott 1988 for discussions of the Ar mini-arc as a deep UV radiometric standard). Ar mini-arcs, when used without a window at wavelengths > 2000 Å, have exceptional short- and long-term stability as radiometric standards. A small commercially-manufactured, sealed HCD lamp was used during measurements with the 1.0 m Acton spectrometer system.

Every possible transition between known energy levels of Hf II satisfying both the parity change and $\Delta J = -1$, 0, or 1 selection rules was studied during analysis of FTS data. Energy levels from Moore (1971) were used to determine possible transition wave numbers. A subset of the Hf II energy levels have been improved to interferometric accuracy by Lundqvist et al. (2006), but the older values from Moore are not seriously in error.

We set baselines and integration limits "interactively" during analysis of the FTS spectra. The same numerical integration routine was used to determine the un-calibrated intensities of Hf II lines and selected Ar I and Ar II lines used to establish a relative radiometric calibration of the spectra. A simple numerical integration technique was used in this and most of our other recent studies because of weakly resolved or unresolved hyperfine and isotopic structure. More sophisticated profile fitting is used only when the line sub-component structure is either fully resolved in the FTS data or known from independent measurements.

The procedure for determining branching fraction uncertainties was described in detail by Wickliffe et al. (2000). Branching fractions from a given upper level are defined to sum to unity, thus a dominant line from an upper level has small branching fraction uncertainty almost by definition. Branching fractions for weaker lines near the dominant line(s) tend to have uncertainties limited by their S/N ratios. Systematic uncertainties in the radiometric calibration are typically the most serious source of uncertainty for widely separated lines from a common upper level. We used a formula for estimating this systematic uncertainty that was presented and tested extensively by Wickliffe et al. (2000). The highest current spectrum of the HCD lamp enabled us to connect the stronger visible and near IR branches to quite weak branches in the same spectral range. Uncertainties grew to some extent from piecing together branching ratios from so many spectra, but such effects have been included in the uncertainties on branching fractions of the weak visible and near IR lines. In the final analysis, the branching fraction uncertainties are primarily systematic. Redundant measurements with independent radiometric calibrations help in the assessment of systematic uncertainties. Redundant measurements from spectra with different discharge conditions also make it easier to spot blended lines and optically thick lines.

Branching fractions from the FTS spectra were combined with the radiative lifetime measurements described in §2 to determine absolute transition probabilities for 150 lines of Hf II in Table 3. Air wavelengths in Table 3 were computed from energy levels (Moore 1971) using the standard index of air (Edlén 1953).

Transition probabilities for the very weakest lines that were observed with poor S/N ratios (branching fractions < 0.001), and for a few blended lines, are not included in Table 3; however these lines are included in the branching fraction normalization. The effect of the problem lines becomes apparent if one sums all transition probabilities in Table 3 from a chosen upper level, and compares the sum to the inverse of the upper level lifetime from Table 1. Typically the sum of the Table 3 transition probabilities is between 98% and 100 % of the inverse lifetime. Although there is significant fractional uncertainty in the branching fractions for these problem lines, this does not have much effect on the uncertainty of the stronger lines that were kept in Table 3. Branching fraction uncertainties are combined in quadrature with lifetime uncertainties to determine the transition probability uncertainties in Table 3. Possible systematic errors from missing branches to unknown lower levels are negligible in Table 3, because we were able to make at least rough measurements on visible and near IR lines with branching fractions as small as 0.001. The generally short Hf II lifetimes, in combination with the frequency cubed scaling of transition probabilities, means that any unknown line in the mid- to far-IR region will not have a significant branching fraction.

The recently published work by Lundqvist et al. (2006) provides a valuable opportunity for comparing at least some of our branching fraction measurements to independent, modern branching fraction measurements. Branching fraction uncertainties are primarily systematic, not statistical. It has, in most comparisons, not been possible for independent research groups to achieve the level of agreement in branching fraction measurements that is routinely achieved in LIF radiative lifetime measurements (e.g. Lawler et al. 2006). Both our branching fraction experiment and the experiment by Lundqvist et al. employed high

performance FTS's. The Chelsea Instruments FT 500 at Lund University has better deep UV performance than the 1.0 m FTS at Kitt Peak, but there is enough overlap between our UW experiment and the Lund experiment for a meaningful comparison. The two experiments utilized different spectrometers, different lamps, and different analysis software. There is, however, some overlap in calibration technique. Lundqvist et al. used the Ar line technique for wavenumbers below $30,000 \text{ cm}^{-1}$ (wavelengths above 3333 Å) and a D₂ standard lamp for wavenumbers above $27,800 \text{ cm}^{-1}$ (wavelengths below 3597 Å). This comparison cannot be considered to be a test of the Ar I and Ar II calibration lines, but as mentioned above there have been multiple independent test of the Ar branching ratios. Figure 1 is a plot of the branching fractions from the Lund University effort divided by our University of Wisconsin (UW) branching fraction as a function of wavelength for 72 transitions from eight upper levels. Figure 2 is a similar plot as a function of the UW branching fraction. The error bars in this plot were determined by combining in quadrature the UW relative branching fraction uncertainty with the relative Lund transition probability uncertainty. Lundqvist et al. did not report separate branching fraction uncertainties. For a weaker line the branching fraction uncertainty typically dominates the transition probability uncertainty, but for strong lines the lifetime uncertainty dominates the transition probability uncertainty. This means that the error bars are somewhat larger than desired for the strong UV transitions. The comparison reveals good (single error bar) agreement on all but a few branching fractions. If the data Figure 1 is replotted with points of similar wavelength averaged together, then a weak dependence on wavelength becomes visible. This wavelength dependence is probably due to slightly (10% to 15%) different radiometric calibrations over the 3000 to 6500? range. Such differences over more than a factor of 2 in wavelength are consistent with estimated uncertainties in the calibration techniques. A close inspection of Figure 2 reveals greater discordance for the weaker branches. This is expected in part because uncertainty migrates to the weaker branches by the definition of a branching fraction as discussed above. The weaker branches are also more vulnerable to line blending errors and S/N limitations.

Figure 3 is a comparison of $\log(gf)$ values from the Lund University study to our (UW) $\log(gf)$ values with Delta $\log(gf) = \log(gf)_{Lund} - \log(gf)_{UW}$ plotted as a function of $\log(gf)_{UW}$. The effect of the slight differences in radiative lifetime measurements on the longer lived levels as discussed in § 2 is visible; the average Delta $\log(gf)$ is clearly less than zero. Never-the-less most of the Delta $\log(gf)$ are within one error bar of zero. Lundqvist et al. (2006) compared their measurements to $\log(gf)$ values from the beam foil study by Andersen et al. (1976) and to $\log(gf)$ values from the arc emission study by Corliss & Bozman (1962). We omit those comparisons here, since the above comparison to Lundqvist et al.'s results from laser and FTS measurements is the most relevant.

4. SOLAR AND STELLAR HAFNIUM ABUNDANCE

We have employed the new Hf $\scriptstyle\rm II$ transition probabilities to re-determine the hafnium abundance of the solar photosphere, and to derive its abundance in 10

very metal-poor ([Fe/H] \leq -1.5)² stars that have large overabundances of the rare-earth elements (e.g., [Eu/Fe] \geq +0.5). Our analyses followed the methods used in previous papers of this series (in particular Lawler et al. 2006 and Den Hartog et al. 2006, hereafter DLSC06).

4.1 Line Selection

We have determined accurate transition probabilities for 150 Hf II lines, but unfortunately very few of these can be used in abundance analyses of the Sun and cool metal-poor stars. This can be understood by considering line strength factors for the Hf II transitions. In a standard LTE abundance analysis the relative strengths of lines of individual species vary directly as the product of elemental abundances, transition probabilities, Saha ionization corrections, and Boltzmann excitation factors. For Hf II, like all of the nearby rare-earth first ions, the problem is simplified, because the ionization potential is relatively low (6.825 eV for Hf, Grigoriev & Melikhov 1997). In photospheres of the Sun and red giant stars all these elements are completely ionized, or $n_{II} \approx n_{total}$. Therefore Saha corrections to account for other ionization state populations are very small and can be ignored. Then for a weak line on the linear part of the curve-of-growth, the equivalent width (EW) and reduced width (RW) are related as $\log(RW) \equiv \log(EW/\lambda) \propto \log(\epsilon gf) - \theta \chi$, where ϵ is the elemental abundance, gf is the oscillator strength, χ is the excitation energy in units of eV, and $\theta \equiv 5040/T$ is the inverse temperature. We thus define the relative strength factor of a transition, ignoring line saturation effects, as STR $\equiv \log(\epsilon q f) - \theta \chi$. Ionized-species transitions of elements with low first ionization potentials can be reliably inter-compared with these strength factors.

In Figure 4 we plot Gd II and Hf II line strength factors as a function of wavelength. The left-hand panel, showing Gd II data, is identical to the right-hand panel of Figure 2 in DLSC06. The right-hand panel of Figure 4 is generated from the Hf II data of this paper. For these computations we have assumed $\theta = 1.0$, a compromise value between that of the Sun ($T_{eff} = 5780$ K or $\theta = 0.87$) and metal-poor giants ($T_{eff} \approx 4600$ K or $\theta \approx 1.10$). The exact value of θ is not important for our purposes, since the vast majority of measurable Gd II and Hf II lines in the Sun and metal-poor stars of interest here arise from low excitation energy states, $\chi < 1$ eV). We have adopted approximate solar abundances of log $\varepsilon(\mathrm{Gd}) = +1.1$ (DLSC06), and log $\varepsilon(\mathrm{Hf}) = +0.9$ (close to the photospheric value suggested by, e.g., Lodders 2003, which we will confirm in this study).

In Figure 4 we have also indicated the approximate strength factors for extremely weak Gd II and Hf II lines in the solar spectrum, and for lines that are reasonably strong. The assignment of these strength levels is discussed in detail by DLSC06. Briefly, the very weak line strength level was estimated by first assuming that the weakest unblended lines routinely measurable on the Delbouille et al. (1973) center-of-disk solar spectrum have $EW_{weak} \approx 1.5 \text{ mÅ}$

 $^{^2 \}text{We}$ adopt standard stellar spectroscopic notations that for elements A and B, [A/B] = $\log_{10}(N_A/N_B)_{star}$ - $\log_{10}(N_A/N_B)_{sun}$, for abundances relative to solar, and log $\varepsilon(A) = \log_{10}(N_A/N_H) + 12.0$, for absolute abundances.

in the blue spectral region ($\lambda \sim 4500$ Å), or $\log(\mathrm{RW})_{weak} \approx -6.5$. Repeated searches for weak lines of Sm II (Lawler et al. 2006) and Gd II (DLSC06) indicated that $\log(\mathrm{RW})_{weak} \approx -6.5$ corresponds to $\mathrm{STR}_{weak} \approx -0.6$. This veryweak-line strength estimate will also apply to Hf II transitions. The strong-line strength value was more arbitrarily set at a value 20 times larger, or $\mathrm{STR}_{strong} = -0.6 + 1.3 = +0.7$. If lines remained unsaturated then their equivalent widths would scale linearly: $\log(\mathrm{RW})_{strong} \approx -5.2$, or $\mathrm{EW}_{strong} \approx 30$ mÅ near 4500 Å. Lines of this strength are somewhat saturated, such that in the solar spectrum $\mathrm{STR} \approx 0.7$ corresponds to $\log(\mathrm{RW}) \approx -5.35$, or $\mathrm{EW} \approx 20$ mÅ at 4500 Å.

To summarize the above discussion, lines of Sm II, Gd II, and Hf II (as well as lines of other ionized rare-earth elements) with STR \approx -0.6 are so weak that they are difficult to detect in the solar spectrum, and those with STR > +0.7 are strong. Using these line-strength criteria, Gd II has about 250 potential lines for solar abundance analyses, and nearly 50 strong lines. In contrast, as is obvious from Figure 4, Hf II simply has very few promising transitions: only 21 lines with STR > -0.6, and no strong lines at all. These numbers are qualitatively consistent with solar spectrum identifications given by Moore, Minnaert, & Houtgast (1966): 60 lines of Gd II but only 18 of Hf II.

We repeated the procedures described in DLSC06 and earlier papers of this series to identify the final set of Hf II lines to be used in the solar/stellar abundance analyses. Having relatively few potential Hf II lines, we carefully considered all with STR > -1.5. From visual comparison of the electronic version of the Delbouille et al. (1973) solar center-of-disk spectrum with the spectrum of the r-process-rich metal-poor giant star BD +17°3248 (Cowan et al. 2002), and from review of the Moore et al. (1966) solar line identifications, we eliminated the completely unsuitable lines: those that are undetectably weak and/or severely blended in both of these spectra. We then consulted the Kurucz (1998) atomic and molecular line compendium, in order to eliminate remaining candidate lines that suffer significant contamination by transitions of other neutron-capture species. In the end only 19 Hf II lines survived to be subject to closer inspection in solar and/or stellar spectra.

4.2 The Solar Photospheric Hafnium Abundance

We employed synthetic spectrum computations following procedures discussed by DLSC06. Atomic and molecular line lists in 4 to 6 Å intervals surrounding each Hf II transition were compiled from Kurucz's (1998) line database and Moore et al.'s (1966) solar identifications. These line lists and the Holweger & Müller (1974) solar model atmosphere were used as inputs into the current version of the LTE line analysis code MOOG (Sneden 1973) to generate the synthetic spectra. The Solar atmospheric model parameters are listed in Table 4. We assumed the solar photospheric abundances recommended in reviews by e.g, Grevesse & Sauval (1998, 2002) and Lodders (2003), as well as values for neutron-capture elements determined in earlier papers of this series. Transition probabilities for ionized species of neutron-capture elements were taken from

 $^{^3{\}rm Available~at~http://bass2000.obspm.fr/solar_spect.php}$

these recent studies: Y, Hannaford et al. (1982); Zr, Malcheva et al. (2006); La, Lawler et al. (2001a); Ce, Palmeri et al. (2000); Pr, Ivarsson et al. (2001); Nd, Den Hartog et al. (2003); Sm, Lawler et al. (2006); Eu, Lawler et al. (2001b); Gd, DLSC06; Tb, Lawler et al. (2001c); Dy, Wickliffe et al. (2000); Ho, Lawler et al. (2004); and Hf, the present work.

We computed multiple synthetic spectra for the 19 selected Hf lines, and compared them to the Delbouille et al. (1973) photospheric spectrum. The synthetic spectra were smoothed with a Gaussian to match the observed line broadening (from photospheric macroturbulence and instrumental effects). As in previous papers in this series, predicted contaminant absorptions were matched to the solar spectrum by: (a) altering oscillator strengths for known atomic transitions, except for the species listed above; (b) varying the abundances of C, N, and/or O for CH, CN, NH, and OH band lines: and (c) adding Fe I lines with excitation potentials $\chi=3.5$ eV and arbitrary transition probabilities for unknown absorptions. After modifications of the line lists to match the solar spectrum, similar trials were also performed for BD +17°3248. These initial synthetic spectrum computations demonstrated that 7 of the 19 proposed Hf II lines were useless for abundance determinations in the Sun and even in the most r-process-rich of the metal-poor stars discovered to date. The final set of 12 Hf II lines remaining after these tests is listed in Table 5.

In the solar photospheric spectrum we found just four Hf II features to be good hafnium abundance indicators. These are displayed in Figure 5. Inspection of this figure illustrates the analytical problems discussed above: the Hf II lines are all weak and blended to varying degrees. In fact, only the 4093.15 Å line (panel a) is largely unblended and occurs in a wavelength region interval where the solar continuum can be defined reasonably well. The 3918.09 Å line (panel b) has a weak local blend by Co I 3918.06 Å, but more importantly the continuum level is defined by an Fe I blend near 3918.5 Å and an extremely strong Fe I line at 3920.26 Å. The 3561.66 Å line (panel c) should be one of the strongest Hf II transitions; see Figure 4. In reality it is a minor constituent of the blend dominated by Ti II 3561.58 Å and Ni I 3561.76 Å. Finally, the 3389.83 Å line (panel d) is clearly present, but its intrinsic weakness and proximity to the strong Fe I 3389.75 Å line renders it useful only in confirming the hafnium abundance determined from the other features.

Abundances derived for these Hf II lines are listed in Table 5. A straight mean abundance is $\log \varepsilon(\mathrm{Hf}) = 0.88 \pm 0.02$ ($\sigma = 0.03$), where σ is one standard deviation of the set of measurements. The formal scatter figure surely must underestimate the actual internal errors, because the synthetic/observed spectrum fitting procedures needed several judgment decisions to account for significant line blending issues for all but the 4093 Å line. Repeated test syntheses of the four lines, altering various feature contamination and continuum placement assumptions, suggest that a more conservative estimate of $\log \varepsilon(\mathrm{Hf}) = 0.88 \pm 0.08$ is appropriate if all four lines are given equal weight. If the hafnium abundance were to be based only on the 4093 Å line then we estimate $\log \varepsilon(\mathrm{Hf}) = 0.86 \pm 0.05$.

Since Hf II lines arise from ionization/excitation conditions that are very

similar to those of nearby rare-earth species studied in this series of papers, all the same external (scale) errors discussed by DLSC06 for Gd II apply here. The hafnium abundance varies directly with the Hf II partition, but the polynomial representation of Irwin (1981) agrees well with our calculations from currently-available energy level data as discussed in § 3. Within the analysis assumptions of LTE and plane-parallel model atmospheric geometry, the choice of solar model photosphere (e.g., Kurucz 1998 or Grevesse & Sauval 1999 instead of the Holweger & Müller 1974 model used here) changes the derived hafnium abundance by only 0.01 to 0.02 dex. Application of more rigorous modeling of the atomic and solar atmospheric physics should be done in the future, for hafnium and the nearby rare-earth elements.

Andersen et al. (1976) performed the most comprehensive previous solar hafnium abundance study. They derived $\log \varepsilon(\mathrm{Hf}) = 0.88 \pm 0.08$ from eight Hf II transitions, obviously in excellent agreement with our result. They used their own Hf II lifetime data to correct the transition probabilities of Corliss & Bozman (1962), and employed synthetic spectra in their solar abundance analysis. Our lab analysis includes all of their lines, for which our transition probabilities are systematically lower: $\Delta \log(gf) = -0.10$, in the sense this study minus Andersen et al. A simple correction to their abundance would shift it to $\log \varepsilon(\mathrm{Hf}) = 0.98$. However, our solar analysis suggests that most of the Andersen et al. lines are too blended to yield good solar hafnium abundances. Only the 3389 and 3561 Å lines are in common with the present work, and these are our two less reliable lines. Using just these lines, updating the Andersen et al. gf's to our values, would yield $\log \varepsilon(\mathrm{Hf}) = 0.96$, not in serious disagreement with our work.

The Lundqvist et al. (2006) laboratory Hf II study did not perform a detailed solar abundance analysis. Their transition probability scale is smaller than that of Andersen et al. (1976): $\Delta \log(gf) \approx -0.15$. This led them to suggest that the Andersen et al. solar hafnium abundance, "... may be underestimated by 0.1 and 0.2 dex", i.e. $\log \epsilon(\mathrm{Hf}) \approx 1.0$. Direct application of the Lundqvist et al. gf's to our solar abundance analysis is not possible because none of our four photospheric transitions were included in their work. If the generally small mean offset between their transition probability scale and ours were applied to these lines, our photospheric abundance would become $\log \varepsilon(\mathrm{Hf}) = 0.88 + 0.04 = 0.92$, in agreement with our recommended value within the uncertainties of our study and theirs.

The photospheric hafnium abundance is somewhat larger than the current best meteoritic estimates, e.g, $\log \varepsilon(\mathrm{Hf}) = 0.77 \pm 0.04$ (Lodders 2003), but the error bars of the two values do overlap. We will consider the consequences of this small discrepancy in §5.

4.3 Hafnium Abundances in Metal-Poor, r-Process-Rich Stars

We have determined hafnium abundances in 10 very metal-poor giant stars that are known to be enriched in products of r-process nucleosynthesis. In past papers of this series we have only analyzed three extreme cases, CS 22892-052,

BD +17°3248, and HD 115444. However, hafnium is an important element in connecting the lightest rare-earth elements (e.g. La, Z = 57) with elements of the $3^{rd}r$ -process peak (Os, Ir, Pt, Z = 76 to 78). To our knowledge, hafnium is the heaviest (Z = 72) stable element represented by low-excitation (χ < 1.5 eV) ionized lines in cool, metal-poor stellar spectra. The rare earths and the long-lived chronometer elements Th and U also are detected only via these types of transitions. Derived abundance ratios Th/(rare earth) and Hf/(Th or U) are largely insensitive to uncertainties in model atmosphere parameters including: effective temperature, gravity, microturbulent velocity, and overall metallicity. Therefore we have expanded the star list to include 10 r-process-rich stars that have been studied in other abundance surveys (Burris et al. 2000, Simmerer et al. 2004, Cowan et al. 2005).

We determined Hf abundances from as many of the 12 candidate lines as possible for each of the program stars in the same manner as was done for the Sun. In Table 4 we list the model atmosphere parameters and their sources. The individual Hf II line abundances are listed in Table 5. The mean Hf abundances, uncertainties, and number of lines used are listed in Table 6.

We also list mean abundances for La and Eu in Table 6. For HD 221170, BD +17°3248, and CS 22892-052 these values were adopted from the original papers. For the remaining stars we chose to re-derive La and Eu abundances from synthetic spectrum analyses of up to nine La II and six Eu II lines in the spectral region 3700 Å < λ < 4450 Å. Atomic data for the La and Eu transitions were taken from Lawler et al. (2001a) and Lawler et al. (2001b), respectively. The new abundances are in good agreement with previously published values. There are six stars in common with Simmerer et al. (2004). Defining differences in the sense this study minus Simmerer et al., we find Δ log ε (La) = -0.06 \pm 0.02 (σ = 0.06), Δ log ε (Eu) = -0.01 \pm 0.02 (σ = 0.04), and Δ log ε (La/Eu) = -0.04 \pm 0.01 (σ = 0.03). For CS 31082-001, Δ log ε (La/Eu) = -0.06 with respect to the comprehensive Hill et al. (2002) work. Finally, for HD 115444 we find Δ log ε (La/Eu) = -0.03 with respect to Westin et al. (2000); note that their work on this star predates publication of the improved transition probability data for La and Eu.

Few Hf abundances have been derived for very metal-poor stars. Lundqvist et al. (2006) comment on the application of their Hf II gf-values to previous work on two very metal-poor r-process-rich stars, but do not perform independent new analyses. Adjusting the Hill et al. (2002) and Sneden et al. (2003) abundances for CS 31082-001 and CS 22892-052, they recommend $\log \varepsilon(\mathrm{Hf}) = -0.90$ and -0.75 respectively. Our new values of -0.88 and -0.72 (Table 6), are clearly in good agreement with the Lundqvist et al. recommendations.

5. r-PROCESS NUCLEOSYNTHESIS AND HAFNIUM ABUNDANCES

Abundances of neutron-capture elements in low metallicity stars, formed early in the history of the Galaxy, are predominantly the result of r-process nucleosynthesis. The site for this synthesis process is presumably supernova explosions of high-mass (short-lived) stars. In contrast, slow (or s-process)

nucleosynthesis occurs in low-mass (and long-lived) stars (see Cowan & Sneden 2006 for discussion). The r-process rich ejecta from early supernovae were thus injected into the interstellar medium relatively shortly before the formation of the observed (very low metallicity) halo stars. It took much longer for the s-process material to be incorporated into gas that formed somewhat younger and higher metallicity stars (Burris et al. 2000; Simmerer et al. 2004).

The relative neutron-capture abundance distributions exhibit clear star-to-star consistency in very metal-poor halo stars. This has suggested, for example, a robust r-process operating over billions of years and a unique site, or at least a unique set of synthesis conditions for these elements (Cowan & Sneden 2006). Abundance determinations, particularly from high S/N spectra coupled with very precise atomic data, and comparisons among the halo stars can therefore provide critical new information about the synthesis mechanisms and sites for the r-process. Furthermore, since the halo distributions appear to be scaled solar r-process, these abundance comparisons can be employed to constrain the r-process and s-process-only solar system distributions.

5.1 Solar and Stellar Abundance Comparisons

In the 10 r–process rich stars in our sample, hafnium exhibits near-constant abundances with respect to La and Eu: $\log \varepsilon(\mathrm{Hf/La}) = -0.13 \pm 0.02$ ($\sigma = 0.06$) and $\log \varepsilon(\mathrm{Hf/Eu}) = +0.04 \pm 0.02$ ($\sigma = 0.06$). We show the variation of $\log \varepsilon(\mathrm{La/Eu})$ in Figure 6 and $\log \varepsilon(\mathrm{Hf/Eu})$ in Figure 7 as a function of [Fe/H] and [Eu/H]. The star-to-star scatter for both $\log \varepsilon(\mathrm{La/Eu})$ and $\log \varepsilon(\mathrm{Hf/Eu})$ is consistent with observational/analytical uncertainties. No trends with metallicity or overall r-process enhancement are obvious, probably partly as a consequence of the selection of the (mostly all very low-metallicity) stars to include here.

We first consider $\log \varepsilon(\text{La/Eu})$ as a function of metallicity in Figure 6. We have chosen our target stars to be r-process rich. One such indication of this is the value of $\log \varepsilon(\text{La/Eu})$. While La is predominantly an s-process element in solar material, at early Galactic times prior to the onset of the bulk of s-process production, La was synthesized in the r-process. Typical values for r-process rich stars are found to be $\log \varepsilon(\text{La/Eu}) \approx 0.1$, while in solar system material (with a large s-process contribution to La) this value is typically about 0.7 (Simmerer et al. 2004, Cowan et al. 2006). It is seen in Figure 6 that there is a consistency of values for the 10 target stars, with an average of 0.17 (indicated by the solid line) - a clear indication of the r-process rich nature of these stars. We note that some of our stars have metallicities larger than -2. Some evidence has been found for the s-process at metallicities as low as -2.5, although the bulk of Galactic sprocess nucleosynthesis appears to occur closer to $[Fe/H] \ge -2$ (Burris et al. 2000, Simmerer et al. 2004). We have examined $\log \varepsilon(\text{La/Eu})$ for 5 of the most metal-poor ([Fe/H] < -2.5) stars and find almost no difference in average value with respect to that found for all 10 of the target stars. For comparison we also show in this figure a range of previous predictions for the r-process-only log $\varepsilon(\text{La/Eu})$. The lowest dotted line in the figure is a determination based upon earlier deconvolutions of the Solar System

abundances into r- and s-abundances (Simmerer et al. 2004, Cowan et al. 2006). These elemental separations are obtained by first determining individual isotopic s-process contributions in the so called classical model approximation (Käppeler et al. 1989) or a more complicated stellar model approach (Arlandini et al. 1999). (Nuclear data, such as neutron-capture cross sections, can in general be obtained for the s-process nuclei as they are close to stability and have relatively long half-lives. In contrast r-process nuclei are so radioactive and have such short half-lives, that in general, their nuclear properties cannot now be experimentally determined.) The r-process isotopic abundances are then obtained by subtracting the calculated s-process isotopic abundances from the total solar system abundances, and the elemental r-process-only distributions are just the sums of the isotopic contributions. Thus, the r-process abundances are actually residuals and depend very sensitively on the s-process determinations. Also included in the range of values for the predicted r-process-only log $\varepsilon(\text{La/Eu})$ are those determined based upon recent neutron cross section measurements of ¹³⁹La from O'Brien et al. (2003) and Winckler et al. (2006) – the latter denoted by the topmost dotted line in Figure 6.

In Figure 7 we show a similar plot of log $\varepsilon(\mathrm{Hf/Eu})$ for our target stars. In this case we find a mean value of log $\varepsilon(\mathrm{Hf/Eu})=0.04$. Employing only the most metal-poor stars, again makes almost no difference in this average. The dotted line indicates the r-process predicted ratio from Simmerer et al. (2004) and Cowan et al. (2006).

Despite the consistency of the abundance data in the halo stars with the scaled solar system r-only distribution, it is seen in both Figures 6 and 7 that these previous determinations of the (published) solar system r-only values fall below the log $\varepsilon(el/Eu)$ abundance ratios for our 10 sample stars. This suggests a reexamination of the r-only-values for $\log \varepsilon(Hf/Eu)$ and $\log \varepsilon(La/Eu)$ is required employing the more accurate halo abundance determinations, based upon the newly measured and more precise atomic lab data. These abundance data can be utilized to determine directly the solar system r-only values, as opposed to obtaining residuals as described above. Analogously to what was done in DLSC06, we have first averaged the log $\varepsilon(el/Eu)$ offsets (log $\varepsilon(La/Eu)$ in Figure 6 and $\log \varepsilon(Hf/Eu)$ in Figure 7). Europium was used for comparison as it is formed almost entirely in the r-process, in contrast to La and Hf which have significant contributions from the s-process (Simmerer et al. 2004). In this manner, we determined the expected solar system r-only values for both La and Hf. The mean values of the ratios for $\log \varepsilon(\text{La/Eu})$ and $\log \varepsilon(\text{Hf/Eu})$ in the 10 stars are shown in the figures with a solid line. Previous determinations of the individual r-process and s-process contributions for La ($N_r = 0.11$ and $N_s = 0.337$) and Hf ($N_r = 0.081$ and $N_s = 0.076$) (based upon the $N_{Si} = 10^6$ scale) have been listed by Cowan et al. (2006). We find, utilizing the halo star abundances, that the values of N_r should be revised slightly upward such that $N_r = 0.134$ for La and $N_r = 0.099$ for Hf. Summing these r-process predicted contributions with the previously determined s-process values yields total solar abundances of $N_{tot} = 0.471$ (log $\varepsilon = 1.21$) and 0.175 (log $\varepsilon = 0.782$) for La and Hf respectively, again based on the $N_{Si} = 10^6$ scale. The predicted solar system total values for $\log \varepsilon(\text{La/Eu})$ and $\log \varepsilon(\text{Hf/Eu})$ are shown in Figures 6 and 7 as dashed lines. We estimate that the observational and analytic errors probably limit our results to the order of \pm 10%. We note that the value we find for the total Hf abundance using this technique, $\log \varepsilon(\text{Hf}) = 0.782$, is almost identical to that listed by Lodders (2003) for the meteoritic and recommended solar abundance for this element, $\log \varepsilon(\text{Hf}) = 0.77 \pm 0.04$. Both values are somewhat below the published photospheric and our new determination, $\log \varepsilon(\text{Hf}) = 0.88 \pm 0.08$, using a purely spectroscopic approach. In the case of $\log \varepsilon(\text{La/Eu})$ our predicted total = 0.71 compares well with the Lodders (2003) value (0.66) and our observed average solar ratio reported in this paper of 0.62.

In attempting to employ the halo stars for determining the r-process-only elemental values we are assuming that there are no s-process contributions. Previous studies have demonstrated remarkable consistencies between the detailed stellar abundance distributions (for Ba and above) with the solar system r-only distribution – there appear to be no s-process contributions and none would be expected from the main s-process coming from long-lived, low-mass stars (see Cowan and Sneden 2006 and references therein). While the weak s-process (resulting from the capture of neutrons on iron seed nuclei during core helium burning in massive stars) can contribute to the lighter elemental abundances (up to approximately Zr) in solar metallicity stars, this mechanism is not effective in very low-metallicity stars (Pignatari et al. 2006).

5.2 Hafnium and Nucleocosmochronometry Studies

Long-lived radioactive elements such as Th and U can be employed to determine the ages of the oldest stars. Ideally, having the ratio of Th/U would provide the most reliable chronometer. However, despite the detection of U in CS 31082-001 (Cayrel et al. 2001) and the probable detection of U in BD +17°3248 (Cowan et al. 2002), U is difficult to detect – it is inherently weak and the atomic line is often blended with broader molecular lines. Th/Eu has been employed for a number of radioactive-age studies, but the wide separation in mass number (151 to 153 versus 232) and the (possible) associated differences in nucleosynthesis origin has been considered a problem for sometime (see recent discussion in Ivans et al. 2006 and references therein). In at least one case (i.e., CS 31082-001) Th/Eu also gives an unrealistic age estimate (Hill et al. 2002, Schatz et al. 2002). The heaviest stable elements, nearby to the actinides, are the third r-process peak elements Os, Ir, and Pt and the heavier elements Pb and Bi. Together, these could be employed in chronometer pairs. Unfortunately, these elements are difficult to observe from the ground and Bi has not been detected in any metal-poor (r-process rich) field halo star.

Recent theoretical work (Kratz et al. 2006), designed to reproduce the total solar system r-process abundance distribution, has found that the predicted abundances of inter-peak element Hf (Z = 72, A = 176 to 180) follow closely those of third-peak elements (Os through Pt) and Pb. Thus, Hf, observable from the ground, offers promise as a heavy stable element in a chronometer pair such as Th/Hf. Therefore, the newly determined Hf abundances in these 10 halo

stars, many of which also have detectable Th, could be employed to determine more accurate stellar ages.

6. CONCLUSIONS

Hafnium (Z = 72) is well suited to be used as a stable reference element in nucleocosmochronometry based on the unstable elements Th (Z = 90) and U (Z = 92) whose radioactive decay timescales are well determined. Hafnium is heavier than alternate reference elements such as Nd (Z = 60) and Eu (Z =63) and is significantly closer to the $3^{rd}r$ -process peak (Os, Ir, Pt, Z = 76 to 78). Multiple lines of Hf II are measurable in metal poor halo stars with enhanced r-process abundances. In order to improve Hf abundance determinations, we have performed radiative lifetime measurements using time-resolved laser-induced fluorescence on 41 odd-parity levels of Hf II. These results were combined with branching fractions from Fourier transform spectra to determine absolute atomic transition probabilities for 150 lines of Hf II. Approximately half of our measurements overlap with recent independent transition probability measurements using the LIF plus FTS method and good agreement is found in a detailed comparison. These new laboratory data were applied to (re)determine the Hf abundances of the Sun and 10 metal poor, r-process rich halo stars. Our refined Solar Hf abundance determination, $\log \varepsilon(\mathrm{Hf}) = 0.88 \pm 0.08$, is in agreement with earlier work. The r-process-rich stars possess constant La/Eu and Hf/Eu abundance ratios to within the uncertainties of our analysis; $\log \varepsilon(Hf/La)$ = -0.13 \pm 0.02 (σ = 0.06) and log ε (Hf/Eu) = +0.04 \pm 0.02 (σ = 0.06). The newly determined Hf values set the stage for improved radioactive stellar age determinations using the Th/Hf chronometer pair. The observed average stellar abundance ratio of Hf/Eu and La/Eu is larger than previous estimates of the solar system r-process-only value, suggesting a somewhat larger contribution from the r-process to the production of Hf and La.

ACKNOWLEDGMENTS

We thank K. Lodders for helpful discussion. This work is supported by the National Science Foundation under grants AST- 0506324 (JEL and EADH), AST-0307495 (CS), and AST-0307279 (JJC). J. E. Lawler is a guest observer at the National Solar Observatory and he is indebted to Mike Dulick and Detrick Branstron for help with the 1 m Fourier transform spectrometer.

REFERENCES

Adams, D. L., & Whaling, W. 1981, J. Opt. Soc. Am., 71, 1036

Andersen, T., Petersen, P., & Hauge, O., 1976, Sol. Phys., 49, 211

Arlandini, C., Käppeler, F., Wisshak, K., Gallino, R., Lugaro, M., Busso, M., & Straniero, O. 1999, ApJ, 525, 886

Biémont, E., Baudoux, M., Kurucz, R. L., Ansbacher, W., & Pinnington, E. H. 1991, A&A, 249, 539

Brault, J. W. 1976, J. Opt. Soc. Am., 66, 1081

Bridges, J. M., & Ott, W. R. 1977, Applied Optics, 16, 367

Burris, D. L., Pilachowski, C. A., Armandroff, T. E., Sneden, C., Cowan, J. J., &

Roe, H. 2000, ApJ, 544, 302

Cayrel, R. et al. 2001, Nature, 409, 691

Cayrel, R. et al. 2004, A&A, 416, 1117

Corliss, C. H., & Bozman, W. R. 1962, Experimental Transition Probabilities for Spectral Lines of Seventy Elements, U. S. Natl. Bur. Standards Monograph 53, (Washington: U. S. Government Printing Office)

Cowan, J. J., Burris, D. L., Sneden, C., McWilliam, A., & Preston, G. W. 1995, ApJ, 439, L51

Cowan, J. J., & Sneden, C. 2006, Nature, 440, 1151

Cowan, J. J., et al. 2002, ApJ, 572, 861

Cowan, J. J., et al. 2005, ApJ, 627, 238

Cowan, J. J., Lawler, J. E., Sneden, C., Den Hartog, E. A., & Collier, J. 2006, To appear in Proc. NASA LAW ed. V. Kwong

Danzmann, K., & Kock, M. 1982, J. Opt. Soc. Am., 72, 1556

Delbouille, L, Roland, G., & Neven, L. 1973, Photometric Atlas of the Solar Spectrum from λ3000 to λ10000, (Liège, Inst. D'Ap., Univ. de Liège)

Den Hartog, E. A., Herd, M. T., Lawler, J. E., Sneden, C., Cowan, J. J., & Beers, T. C. 2005, Ap J. 619, 639

Den Hartog, E. A., Lawler, J. E., Sneden, C., & Cowan, J. J. 2003, ApJS, 148, 543

Den Hartog, E. A., Lawler, J. E., Sneden, C., & Cowan, J. J. 2006, ApJS, in press

Den Hartog, E. A., Wickliffe, M. E., & Lawler, J. E. 2002, ApJS, 141, 255 Den Hartog, E. A., Wiese, L. M. & Lawler, J. E. 1999, J. Opt. Soc. Am. B, 6, 2278

Duquette, D. W., Den Hartog, E. A., & Lawler, J. E. 1986, J. Quant. Spect. Rad. Trans, 35, 281

Edlén, B. 1953, J. Opt. Soc. Am., 43, 339

Gratton, R. G., & Sneden, C. 1994, A&Ap, 287, 927

Grevesse, N., & Sauval, A. J. 1998, Space Sci. Rev., 85, 161

Grevesse, N., & Sauval, A. J. 1999, A&Ap, 347, 348

Grevesse, N., & Sauval, A. J. 2002, Advances in Space Science Res., 30, 3

Grigoriev, I. S., & Melikhov, E. Z. 1997, Handbook of Physical Quantities, (Boca Raton, CRC Press) p. 516

Guo, B., Ansbacher, W., Pinnington, E. H., Ji, Q., & Berends, R. W. 1992, Phys. Rev. A, 46, 641

Hannaford, P, Lowe, R. M., Grevesse, N., Biémont, E., & Whaling, W. 1982, ApJ, 261, 736

Hashiguchi, S., & Hasikuni, M. 1985, J. Phys. Soc. Japan 54, 1290

Hill, V., et al. 2002, A&A, 387, 560

Holweger, H., & Müller, E. A. 1974, Sol. Phys., 39, 19

Irwin, A. W. 1981, ApJS, 45, 621

Ivans, I. I., Simmerer, J., Sneden, C., Lawler, J. E., Cowan, J. J., Gallino, R., & Bisterzo, S. 2006, ApJ, 645, 613

Ivarsson, S., Litzén, U., & Wahlgren, G. M. 2001, Phys. Scr., $64,\,455$

Käppeler, F., Beer, H., & Wisshak, K. 1989, Rep. Prog. Phys., 52, 945

Klose, J. Z., Bridges, J. M., & Ott, W. R. 1988, J. Res. Natl. Bur. Stand., 93, 21

Kono, A., & Hattori, S. 1984, Phys. Rev. A, 29, 2981

Kratz, K. L., Farouqi, K., Pfeiffer, B., Truran, J. W., Sneden, C., & Cowan, J. J. 2006, ApJ, submitted

Kurucz, R. L. 1998, in Fundamental Stellar Properties: The Interaction between Observation and Theory, IAU Symp. 189, ed T. R. Bedding, A. J. Booth and J. Davis (Dordrecht: Kluwer), p. 217

Lawler, J. E., Bonvallet, G., & Sneden, C. 2001a, ApJ, 556, 452

Lawler, J. E., Wickliffe, M. E., Den Hartog, E. A., & Sneden, C. 2001b, ApJ, 563, 1075

Lawler, J. E., Wickliffe, M. E., Cowley, C. R., & Sneden, C. 2001c, ApJS, 137, 341

Lawler, J. E., Sneden, C., & Cowan, J. J. 2004, ApJ, 604, 850

Lawler, J. E., Den Hartog, E. A., Sneden, C., & Cowan, J. J. 2006, ApJS, 162, 227

Lodders, K. 2003, ApJ, 591, 1220

Lundqvist, M., Nilsson, H., Wahlgren, G. M., Lundberg, H., Xu, H. L., Jang, Z.-K., & Leckrone, D. S. 2006, A&A, 450, 407

Malcheva, G., Blagoev, K., Mayo, R., Ortiz, M., Xu, H. L., Svanberg, S., Quinet, P., &

Biémont, E. 2006, MNRAS, 367, 754

McWilliam, A., Preston, G. W., Sneden, C., & Searle, L. 1995, AJ, 109, 2757

Moore, C. E., Minnaert, M. G. J., & Houtgast, J. 1966, *The Solar Spectrum* 2934 Å to 8770 Å, NBS Monograph 61 (Washington: U.S. G. P. O.)

Moore, C. E. 1971, *Atomic Energy Levels*, Nat. Stand. Ref. Data Ser. Nat. Bur. Stand. 35, V. III, (Washington: U. S. Government Printing Office), p. 147

O'Brien, S., Dababneh, S., Heil, M., Käppeler, F., Plag, R., Reifarth, R., Gallino, R., Pignatari, M. 2003, Phys. Rev. C, 68, 035801-035807

Palmeri, P., Quinet, P., Wyart, J.-F., & Biémont, E. 2000, Physica Scripta, 61, 323

Pignatari, M., Gallino, R., Baldovin, C., Wiescher, M., Herig, F., Heger, A., Heil, M., & Käppeler, F. 2006, To appear in the Proceedings of the International Symposium on Nuclear Astrophysics.

Ryan, S. G., Norris, J. E., & Beers, T. C. 1996, ApJ, 471, 254

Schatz, H., Toenjes, R., Pfeiffer, B., Beers, T. C., Cowan, J. J., Hill, V., & Kratz, K-L. 2002, ApJ, 579, 626

Simmerer, J., Sneden, C., Cowan, J. J., Collier, J., Woolf, V.M., & Lawler, J. E. 2004, ApJ, 617, 1091

Sneden, C. 1973, ApJ, 184, 839

Sneden, C. et al. 2003, ApJ, 591, 936

Sneden, C., McWilliam, A., Preston, G. W., Cowan, J. J., Burris, D. L., & Armosky, B. J. 1996, ApJ, 467, 819

Volz, U., & Schmoranzer, H. 1998, in AIP Conf. Proc. 434, Atomic and Molecular Data and Their Applications, ed. P. J. Mohr & W. L. Wiese (Woodbury, NY:AIP), p. 67

Weiss, A. W. 1995, Phys. Rev. A, 51, 1067

Westin, J., Sneden, C., Gustafsson, B., & Cowan, J.J. 2000, ApJ, 530, 783 Whaling, W., Carle, M. T., & Pitt, M. L. 1993, J. Quant. Spectrosc. Rad. Transfer 50, 7

Wickliffe, M. E., Lawler, J. E., & Nave, G. 2000, J. Quant. Spec. Rad. Transfer, 66, 363

Winckler, N., Dababneh, S., Heil, M., Käppeler, F., Gallino, R., & Pignatari, M. 2006, ApJ, 647, 685

Wyart, J-F. & Blaise J. 1990, Phys. Scr., 42, 209

Yan, Z-C, Tambasco, M., & Drake, G. W. F. 1998, Phys. Rev. A, 57, 1652

FIGURE CAPTIONS

Figure 1. Ratio of the Lund University (Lund) branching fraction from (Lundqvist et al. 2006) to the University of Wisconsin (UW) branching fraction from this work as a function of wavelength.

Figure 2. Ratio of the Lund University branching fraction (Lundqvist et al. 2006) to the University of Wisconsin (UW) branching fraction from this work as a function of the UW branching fraction.

Figure 3. Delta $\log(gf) = \log(gf)_{Lund} - \log(gf)_{UW}$ plotted as a function of $\log(gf)_{UW}$.

Figure 4. Relative strength factors, $\log(\varepsilon gf) - \theta \chi$, (\equiv STR) for Gd II and Hf II lines, plotted as functions of wavelength. These factors are discussed in the text in § 4.1. Solar abundances (ε_{Sun}) and an approximate inverse temperature ($\theta = 1.0$) have been assumed in forming these factors. Dotted lines indicate the approximate value of STR for lines near the detection limit in the Sun, and dashed lines indicate minimum STR levels for lines that are strong in the Sun. The left-hand panel is identical to the right-hand panel of Figure 4 in DLSC06. The right-hand panel is generated with data from the present work. In this panel we have shown with circled dots the 12 Hf II lines finally employed in the abundance analyses.

Figure 5. Spectra of the four Hf II lines used in the solar photospheric analysis. The filled circles represent the center-of-disk spectra of Delbouille et al. (1973), but for clarity in the figure we have only shown points spaced every 0.01 Å instead of the original 0.002 Å. The four lines shown in each panel represent the synthetic spectra for which the hafnium abundance has been varied. The synthetic spectrum with weak-to-absent absorption at the Hf II wavelength was computed without any hafnium contribution. The synthetic spectrum that nearly traces the observed one was computed with the log $\varepsilon(\text{Hf})$ value derived for that transition (see Table 5), and the other two syntheses were done with hafnium abundances decreased and increased by a factor of two from the best-fit value. The labeled tick marks in each panel are put at 1 Å intervals, and the unlabeled tick marks are spaced at 0.1 Å.

Figure 6. Abundance comparisons of $\log \varepsilon(\text{La/Eu})$ versus [Fe/H] and [Eu/H] for a group of 10 metal-poor r-process rich stars. The dotted lines define the range of the solar system r-process-only values based upon the published deconvolution of the solar system abundances (Simmerer et al. 2004, Cowan et al. 2006), the solid line is the mean ratio of the 10 halo stars in our sample, and the dashed line is the total solar system ratio based upon the stellar value for the r-process (see text in § 5.1 for details).

Figure 7. Abundance comparisons of log $\varepsilon(Hf/Eu)$ versus [Fe/H] and [Eu/H] for a group of 10 metal-poor r-process rich stars. The lines are similar to those in Figure 6.

Table 1. Radiative lifetimes for odd-parity Hf II levels from LIF measurements.

Level	Configuration a	Term a	J	Laser Wavelengths	Lifet	time (ns)
$(\mathrm{cm}^{-1})^a$				${\rm In} {\rm Air} (\mathring{\rm A})$	This	Other
					Expt.^b	LIF^c
28068.79	$5d6s(a^{3}D)6p$	$\mathrm{z}^4\mathrm{F}^o$	1.5	3561.66, 4093.15	39.4	
29405.12	$5d6s(a^3D)6p$	z^4F^o	2.5	3399.79, 3880.82	26.4	29.7 ± 2.4
33776.24	$5d6s(a^3D)6p$	z^4F^o	3.5	3253.70, 3644.35	32.4	34.8 ± 2.5
38185.67	$5d6s(a^3D)6p$	z^4F^o	4.5	3139.66, 3352.05	47.2	
29160.04	$5d6s(a^3D)6p$	$\mathrm{z}^4\mathrm{D}^o$	0.5	3428.37, 3918.09	43.8	
31784.16	$5d6s(a^3D)6p$	$\mathrm{z}^4\mathrm{D}^o$	1.5	$3145.31,\ 3479.29$	18.9	21.8 ± 1.8
34355.13	$5d6s(a^3D)6p$	z^4D^o	2.5	$3193.53,\ 3255.28$	14.7	16.2 ± 1.4
36882.49	$5d6s(a^3D)6p$	z^4D^o	3.5	$3273.65,\ 3505.22$	16.7	
33136.20	$5d6s(a^3D)6p$	$z^2 P^o$	0.5	$3016.97,\ 3389.83$	17.6	
36373.42	$5d6s(a^3D)6p$	$z^2 P^o$	1.5	$3000.10,\ 3176.85$	17.7	
33180.92	$5d6s(a^1D)6p$	z^2D^o	2.5	$3012.90,\ 3384.70$	16.3	18.1 ± 1.5
34123.93	$5d6s(a^1D)6p$	z^2D^o	1.5	$3217.29,\ 3279.97$	23.3	24.5 ± 2.5
34942.36	$5d^2(a^3F)6p$	$\mathrm{z}^4\mathrm{G}^o$	2.5	$3134.73,\ 3194.20$	8.0	8.4 ± 0.5
38498.53	$5d^2(a^3F)6p$	$\mathrm{z}^4\mathrm{G}^o$	3.5	$2820.23,\ 2975.88$	5.0	5.1 ± 0.3
42391.09	$5d^2(a^3F)6p$	$\mathrm{z}^4\mathrm{G}^o$	4.5	2773.36, 2937.78	4.2	
46209.05	$5d^2(a^3F)6p$	$\mathrm{z}^4\mathrm{G}^o$	5.5	2641.41	3.3	
37885.90	$5d6s(a^3D)6p$	y^2D^o	1.5	$2638.72,\ 2919.60$	3.4	
41761.24	$5d6s(a^3D)6p$	y^2D^o	2.5	$2393.84,\ 2822.68$	2.9	
38398.56	$5d6s(a^3D)6p$	$z^4 P^o$	0.5	3923.90	28.3	
39226.46	$5d6s(a^3D)6p$	$z^4 P^o$	1.5	$3665.35,\ 3883.77$	29.1	
40506.86	$5d6s(a^3D)6p$	$z^4 P^o$	2.5	$2669.01,\ 2808.00$	12.4	
38578.63	$5d6s(a^3D)6p$	z^2F^o	2.5	2813.87, 2968.80	5.2	
41406.86	$5d6s(a^3D)6p$	z^2F^o	3.5	2606.38, 2738.76	5.2	
42518.10	$5d^2(a^3F)6p$	y^4F^o	1.5	$2351.22,\ 2571.68$	2.15	2.3 ± 0.2
43680.75	$5d^2(a^3F)6p$	y^4F^o	2.5	$2460.50,\ 2578.15$	3.2	3.3 ± 0.2
44399.96	$5d^2(a^3F)6p$	y^4F^o	3.5	$2417.70,\ 2531.20$	4.1	
46124.89	$5d^2(a^3F)6p$	y^4F^o	4.5	$2513.03,\ 2647.30$	2.8	
42770.56	$5d6s(a^1D)6p$	$y^2 P^o$	1.5	$2337.34,\ 2516.89$	2.6	2.6 ± 0.2
43044.26	$5d6s(a^1D)6p$	$y^2 P^o$	0.5	$2322.48,\ 2537.33$	1.75	1.8 ± 0.2
43900.56	$5d6s(a^1D)6p$	y^2F^o	2.5	$2447.26,\ 2563.62$	2.7	
44690.72	$5d6s(a^1D)6p$	y^2F^o	3.5	$2512.70,\ 2607.03$	2.7	
45643.25	$5d^2(a^3F)6p$	y^4D^o	0.5	$2380.31,\ 2967.24$	2.40	2.2 ± 0.2
46674.36	$5d^2(a^3F)6p$	y^4D^o	1.5	$2291.64,\ 2323.26$	2.00	2.1 ± 0.2
47904.39	$5d^2(a^3F)6p$	y^4D^o	2.5	$2324.89,\ 2405.42$	2.05	2.0 ± 0.2
48930.75	$5d^2(a^3F)6p$	y^4D^o	3.5	$2347.45,\ 2464.19$	2.10	
46495.37	$5d^2(a^3P)6p$	z^2S^o	0.5	2150.08, 2332.97	2.7	2.7 ± 0.2

Table 1—Continued

Level $(cm^{-1})^a$	Configuration (^a Term ^a	J	Laser Wavelengths In Air (Å)	Lifeti This $\operatorname{Expt.}^b$	ime (ns) Other LIF^c
47157.57 49840.47 47973.56 49005.64 53227.27	$5d^{2}(a^{3}F)6p$ $5d^{2}(a^{3}F)6p$ $5d^{2}(b^{1}D)6p$ $5d^{2}(b^{1}D)6p$ $5d^{2}(b^{1}D)6p$	$z^{2}G^{o}$ $z^{2}G$ $x^{2}D^{o}$ $x^{2}D^{o}$ $w^{2}F^{o}$	3.5 4.5 1.5 2.5 3.5	2449.44, 2576.83 2298.35, 2410.14 2255.17, 2321.16 2266.83, 2343.33 2428.99, 2515.49	3.2 3.1 2.50 2.6 2.55	3.1 ± 0.2

^aEnergy levels, configurations, and terms are from Martin et al. (1978).

 $^{^{\}rm b}{\rm The}$ uncertainty of our measurements is the larger of $\pm 5\%$ or ± 0.2 ns.

^c Lundqvist et al. (2006)

arXiv:astro-ph/0611036v1 1 Nov 2006

Table 2. Fourier transform spectra of Hf hollow cathode discharge lamps used in this study. All were recorded using the 1 m FTS on the McMath telescope at the National Solar Observatory, Kitt Peak, AZ.

Index	Date	Serial Number	Buffer Gas	Lamp Current (mA)	Wavenumber Range (cm^{-1})	Limit of Resolution (cm $^{-1}$	Coadds	Beam Splitter	Filter	Detector ^a	Calibration	b
1	1984 Mar. 20	10	Ar	93	0.00 - 36947	0.053	8	UV		Midrange Si Diode	Ar I & II	
2	1984 Mar. 21	2	Ar	43	14432 - 36081	0.053	8	UV	$CuSO_4$	Midrange Si Diode	Ar I & II	
3	1984 Mar. 21	3	Ar	169	14432 - 36081	0.053	8	UV	$CuSO_4$	Midrange Si Diode	Ar I & II	
4	1984 Nov. 1	1	Ar	160	5922 - 44951	0.064	8	UV	CS 9-54	Midrange Si Diode	Ar I & II	
5	1984 Nov. 1	2	Ar	100	5922 - 44951	0.064	8	UV	CS 9-54	Midrange Si Diode	Ar I & II	
6	1987 Jan. 14	9	Ar	500	8218 - 26091	0.050	8	Visible		S. B. Si Diode	Ar I & II, W Strip Lamp	р
7	1984 Mar. 20	11	Ar	93	0.00 - 22831	0.033	8	UV		Midrange Si Diode	Ar I & II	
8	1984 Mar. 21	1	Ar	42	7491 - 22028	0.033	8	UV	GG 495	Midrange Si Diode	Ar I & II	
9	1984 Mar. 21	4	Ar	42	7491 - 22028	0.033	8	UV	GG 495	Midrange Si Diode	Ar I & II	
10	1984 Nov. 1	3	Ar	100	3170 - 15058	0.022	8	UV	RG 715	InSb	Ar I & II	
11	1984 Nov. 1	4	Ar	180	3170 - 15058	0.022	8	UV	RG 715	InSb	Ar I & II	
12	1987 Jan. 14	10	Ne	330	8218 - 26091	0.050	8	Visible		S. B. Si Diode	W Strip Lamp	
13	1987 Jan. 14	11	Ne	370	3488 - 15017	0.029	8	Visible		InSb	W Strip Lamp	

^aDetectors types include the Midrange Si photodiode, Super Blue (S. B.) Si photodiode, and InSb dectector for the Near IR.

^bRelative radiometric calibrations were based on selected sets of Ar I and Ar II lines and on a Tungsten (W) Strip Lamp calibrated as a secondary radiance standard.

Table 3. Atomic transition probabilities for Hf II organized by increasing wavelength in air, λ_{air} .

$\lambda_{air} \ (m \AA)$	E_{upper} (cm^{-1})	J_{upp}	E_{lower} (cm^{-1})	J_{low}	A-value (10^6 s^{-1})	Log(gf)
2638.72	37885.90	1.5	0.00	1.5	163 ± 11	-0.17
2641.41	46209.05	5.5	8361.76	4.5	295 ± 18	0.57
2773.36	42391.09	4.5	6344.34	3.5	173 ± 9	0.30
2820.23	38498.53	3.5	3050.88	2.5	93 ± 5	-0.05
2861.02	34942.36	2.5	0.00	1.5	27.5 ± 2.0	-0.69
2869.83	37885.90	1.5	3050.88	2.5	6.3 ± 0.8	-1.50
2909.92	34355.13	2.5	0.00	1.5	3.6 ± 0.3	-1.56
2919.60	37885.90	1.5	3644.65	1.5	38.4 ± 2.9	-0.71
2929.64	34123.93	1.5	0.00	1.5	22.1 ± 1.2	-0.94
2937.78	42391.09	4.5	8361.76	4.5	56 ± 3	-0.14
2975.88	38498.53	3.5	4904.85	2.5	50.2 ± 2.8	-0.27
3000.10	36373.42	1.5	3050.88	2.5	13.8 ± 0.8	-1.13
3012.90	33180.92	2.5	0.00	1.5	30.8 ± 1.7	-0.60
3016.97	33136.20	0.5	0.00	1.5	2.92 ± 0.22	-2.10
3031.16	37885.90	1.5	4904.85	2.5	60 ± 4	-0.48
3054.53	36373.42	1.5	3644.65	1.5	3.89 ± 0.21	-1.66
3109.11	38498.53	3.5	6344.34	3.5	47.0 ± 2.8	-0.26
3126.28	36882.49	3.5	4904.85	2.5	0.85 ± 0.07	-2.00
3134.73	34942.36	2.5	3050.88	2.5	43.4 ± 2.3	-0.42
3139.66	38185.67	4.5	6344.34	3.5	3.66 ± 0.22	-1.27
3145.31	31784.16	1.5	0.00	1.5	4.6 ± 0.3	-1.57
3176.85	36373.42	1.5	4904.85	2.5	26.3 ± 1.4	-0.80
3193.53	34355.13	2.5	3050.88	2.5	13.9 ± 0.9	-0.89
3194.20	34942.36	2.5	3644.65	1.5	35.6 ± 1.9	-0.49
3217.29	34123.93	1.5	3050.88	2.5	4.85 ± 0.29	-1.52
3253.70	33776.24	3.5	3050.88	2.5	12.1 ± 0.7	-0.81
3255.28	34355.13	2.5	3644.65	1.5	6.4 ± 0.4	-1.21
3273.65	36882.49	3.5	6344.34	3.5	2.51 ± 0.15	-1.49
3279.97	34123.93	1.5	3644.65	1.5	9.2 ± 0.6	-1.23
3317.99	33180.92	2.5	3050.88	2.5	3.53 ± 0.23	-1.46
3328.21	34942.36	2.5	4904.85	2.5	3.16 ± 0.20	-1.50
3352.05	38185.67	4.5	8361.76	4.5	15.8 ± 0.8	-0.57
3384.70	33180.92	2.5	3644.65	1.5	2.11 ± 0.16	-1.66
3389.83	33136.20	0.5	3644.65	1.5	48.1 ± 2.4	-0.78
3394.58	34355.13	2.5	4904.85	2.5	7.4 ± 0.4	-1.11
3399.79	29405.12	2.5	0.00	1.5	25.6 ± 1.3	-0.57
3421.44	34123.93	1.5	4904.85	2.5	0.76 ± 0.06	-2.27

Table 3—Continued

λ_{air} (Å)	E_{upper} (cm ⁻¹)	J_{upp}	E_{lower} (cm ⁻¹)	J_{low}	A-value (10^6 s^{-1})	Log(gf)
(A)	(6111)		(CIII)		(10 8)	
3428.37	29160.04	0.5	0.00	1.5	5.7 ± 0.4	-1.69
3462.64	33776.24	3.5	4904.85	2.5	1.48 ± 0.09	-1.67
3479.29	31784.16	1.5	3050.88	2.5	13.8 ± 0.8	-1.00
3495.75	34942.36	2.5	6344.34	3.5	9.8 ± 0.8	-0.97
3505.22	36882.49	3.5	8361.76	4.5	49.0 ± 2.5	-0.14
3535.55	33180.92	2.5	4904.85	2.5	19.9 ± 1.3	-0.65
3552.71	31784.16	1.5	3644.65	1.5	11.7 ± 0.6	-1.05
3561.66	28068.79	1.5	0.00	1.5	17.6 ± 0.9	-0.87
3569.03	34355.13	2.5	6344.34	3.5	29.9 ± 1.6	-0.46
3644.35	33776.24	3.5	6344.34	3.5	15.0 ± 0.8	-0.62
3661.04	42391.09	4.5	15084.26	3.5	5.0 ± 0.5	-1.00
3665.35	39226.46	1.5	11951.70	0.5	18.1 ± 0.9	-0.84
3681.38	39226.46	1.5	12070.46	2.5	2.19 ± 0.12	-1.75
3719.28	31784.16	1.5	4904.85	2.5	18.7 ± 1.0	-0.81
3780.09	38398.56	0.5	11951.70	0.5	4.39 ± 0.23	-1.73
3782.78	38498.53	3.5	12070.46	2.5	2.09 ± 0.21	-1.44
3793.38	29405.12	2.5	3050.88	2.5	6.0 ± 0.3	-1.11
3872.55	37885.90	1.5	12070.46	2.5	9.3 ± 1.0	-1.08
3880.82	29405.12	2.5	3644.65	1.5	2.48 ± 0.16	-1.47
3883.77	39226.46	1.5	13485.56	2.5	10.6 ± 0.6	-1.02
3918.09	29160.04	0.5	3644.65	1.5	15.8 ± 0.8	-1.14
3923.90	38398.56	0.5	12920.94	1.5	29.0 ± 1.5	-0.87
3933.65	33776.24	3.5	8361.76	4.5	0.87 ± 0.05	-1.79
3996.80	38498.53	3.5	13485.56	2.5	1.37 ± 0.16	-1.58
4020.25	39226.46	1.5	14359.42	1.5	0.87 ± 0.07	-2.08
4029.16	36882.49	3.5	12070.46	2.5	1.01 ± 0.07	-1.71
4080.44	29405.12	2.5	4904.85	2.5	1.89 ± 0.14	-1.55
4093.15	28068.79	1.5	3644.65	1.5	7.0 ± 0.4	-1.15
4113.56	36373.42	1.5	12070.46	2.5	3.8 ± 0.3	-1.41
4249.33	37885.90	1.5	14359.42	1.5	3.3 ± 0.4	-1.45
4262.74	36373.42	1.5	12920.94	1.5	1.28 ± 0.13	-1.86
4269.70	38498.53	3.5	15084.26	3.5	1.87 ± 0.22	-1.39
4272.86	36882.49	3.5	13485.56	2.5	4.1 ± 0.3	-1.04
4319.51	38398.56	0.5	15254.29	0.5	1.37 ± 0.09	-2.11
4327.52	38185.67	4.5	15084.26	3.5	0.147 ± 0.028	-2.38
4334.64	46209.05	5.5	23145.57	4.5	7.6 ± 1.6	-0.59
4335.15	29405.12	2.5	6344.34	3.5	0.104 ± 0.011	-2.75

Table 3—Continued

$\lambda_{air} \ (ext{Å})$	E_{upper} (cm^{-1})	J_{upp}	E_{lower} (cm^{-1})	J_{low}	A-value (10^6 s^{-1})	Log(gf)
4367.90	36373.42	1 5	19405 56	2.5	2.80 ± 0.28	-1.49
4370.95	34942.36	$\frac{1.5}{2.5}$	13485.56 12070.46	$2.5 \\ 2.5$	3.5 ± 0.4	-1.49 -1.22
4370.95	37885.90		12070.40 15254.29	$\frac{2.5}{0.5}$	3.5 ± 0.4 8.5 ± 1.1	
		1.5			6.0 ± 1.1 1.30 ± 0.11	-1.00 -1.63
4486.13	34355.13 34123.93	2.5	12070.46 12070.46	2.5	1.50 ± 0.11 1.61 ± 0.21	
4533.16		1.5		2.5		-1.70
4541.29	36373.42	1.5	14359.42	1.5	1.79 ± 0.20	-1.65
4573.79	39226.46	1.5	17368.87	2.5	2.07 ± 0.16	-1.59
4586.24	36882.49	3.5	15084.26	3.5	0.42 ± 0.04	-1.98
4605.78	33776.24 34942.36	3.5	12070.46	$\frac{2.5}{2.5}$	0.51 ± 0.04	-1.89
4659.22 4664.14		2.5	13485.56	2.5	0.21 ± 0.03	-2.38
	34355.13	2.5	12920.94	1.5	3.6 ± 0.3	-1.15
4672.44	39226.46	1.5	17830.34	1.5	0.111 ± 0.014 0.172 ± 0.026	-2.84
4715.00	34123.93	1.5	12920.94	1.5		-2.64
4719.11	33136.20	0.5	11951.70 17368.87	0.5	3.3 ± 0.4	-1.65
4731.36	38498.53	3.5		2.5	1.9 ± 0.3 0.20 ± 0.03	-1.29 -2.56
4733.72	36373.42	1.5	15254.29	0.5		
4735.66	33180.92	2.5	12070.46	2.5	0.25 ± 0.04	-2.30
4807.13	38185.67	4.5	17389.06	4.5	0.64 ± 0.07	-1.66
4809.17	38498.53	3.5	17710.72	3.5	0.35 ± 0.06	-2.01
4817.21	42391.09	4.5	21637.97	3.5	2.9 ± 0.4	-1.00
4843.99	34123.93	1.5	13485.56	2.5	0.55 ± 0.08	-2.11
4860.51	38398.56	0.5	17830.34	1.5	0.49 ± 0.05	-2.46
4882.65	38185.67	4.5	17710.72	3.5	0.059 ± 0.011	-2.68
4927.00	33776.24	3.5	13485.56	2.5	0.203 ± 0.023	-2.23
4934.46	33180.92	2.5	12920.94	1.5	1.17 ± 0.16	-1.59
4945.38	33136.20	0.5	12920.94	1.5	0.68 ± 0.09	-2.30 -2.22
4984.76	37885.90	1.5	17830.34	1.5	0.40 ± 0.07	
4999.68	34355.13	2.5	14359.42	1.5	0.63 ± 0.07	-1.85
5034.32	34942.36	2.5	15084.26	3.5	0.26 ± 0.04	-2.23
5040.83	31784.16	1.5	11951.70	0.5	2.51 ± 0.22	-1.42
5058.16	34123.93	1.5	14359.42	1.5	0.33 ± 0.05	-2.29
5075.92	33180.92	$\frac{2.5}{2.5}$	13485.56	2.5	0.34 ± 0.05	-2.10
5128.51	36882.49	3.5	17389.06	4.5	0.82 ± 0.09	-1.59
5187.73	34355.13	2.5	15084.26	3.5	0.74 ± 0.08	-1.75
5194.57	42391.09	4.5	23145.57	4.5	0.35 ± 0.07	-1.85
5214.55	36882.49	3.5	17710.72	3.5	0.062 ± 0.010	-2.69
5260.43	36373.42	1.5	17368.87	2.5	1.73 ± 0.24	-1.54

Table 3—Continued

λ_{air}	\mathbf{E}_{upper}	J_{upp}	\mathbf{E}_{lower}	J_{low}	A-value	Log(gf)
(Å)	(cm^{-1})		(cm^{-1})		(10^6 s^{-1})	
5264.95	37885.90	1.5	18897.64	1.5	4.2 ± 0.7	-1.15
5298.04	34123.93	1.5	15254.29	0.5	3.3 ± 0.5	-1.26
5299.85	31784.16	1.5	12920.94	1.5	0.29 ± 0.03	-2.31
5311.59	33180.92	2.5	14359.42	1.5	2.4 ± 0.4	-1.22
5324.25	33136.20	0.5	14359.42	1.5	1.30 ± 0.19	-1.96
5348.40	33776.24	3.5	15084.26	3.5	0.178 ± 0.022	-2.21
5391.35	36373.42	1.5	17830.34	1.5	0.61 ± 0.10	-1.97
5444.04	38498.53	3.5	20134.94	$\frac{1.5}{2.5}$	1.22 ± 0.23	-1.36
5463.38	31784.16	1.5	13485.56	$\frac{2.5}{2.5}$	0.43 ± 0.05	-2.11
5524.35	33180.92	2.5	15084.26	3.5	0.49 ± 0.09 0.68 ± 0.12	-1.73
5590.69	33136.20	0.5	15254.29	0.5	0.140 ± 0.021	-2.88
5767.19	29405.12	2.5	12070.46	2.5	0.140 ± 0.021 0.156 ± 0.026	-2.33
5801.67	34942.36	$\frac{2.5}{2.5}$	17710.72	3.5	0.190 ± 0.020 0.19 ± 0.04	-2.33 -2.23
5809.53	29160.04	0.5	11951.70	0.5	0.13 ± 0.04 0.42 ± 0.05	-2.23
5842.23	34942.36	2.5	17830.34	1.5	0.42 ± 0.09 0.91 ± 0.16	-1.55
5929.36	38498.53	3.5	21637.97	3.5	0.31 ± 0.10 0.118 ± 0.023	-2.30
6041.46	38185.67	4.5	21637.97	3.5	0.110 ± 0.023 0.127 ± 0.023	-2.36 -2.16
6047.98	31784.16	1.5	15254.29	0.5	0.127 ± 0.028 0.100 ± 0.014	-2.66
6093.14	33776.24	3.5	17368.87	2.5	0.029 ± 0.004	-2.89
6135.68	34123.93	1.5	17830.34	1.5	0.020 ± 0.001 0.061 ± 0.013	-2.86
6156.27	29160.04	0.5	12920.94	1.5	0.110 ± 0.024	-2.90
6202.88	28068.79	1.5	11951.70	0.5	0.021 ± 0.003	-3.32
6222.79	33776.24	3.5	17710.72	3.5	0.021 ± 0.008 0.097 ± 0.018	-2.34
6230.86	34942.36	2.5	18897.64	1.5	0.33 ± 0.06	-1.93
6248.92	28068.79	1.5	12070.46	2.5	0.50 ± 0.09	-1.93
6279.84	29405.12	2.5	13485.56	2.5	0.122 ± 0.021	-2.36
6531.64	33136.20	0.5	17830.34	1.5	0.18 ± 0.03	-2.65
6557.92	36882.49	3.5	21637.97	3.5	0.39 ± 0.07	-1.69
6644.58	29405.12	2.5	14359.42	1.5	0.50 ± 0.08	-1.70
6647.06	38185.67	4.5	23145.57	4.5	0.73 ± 0.12	-1.32
6754.61	29160.04	0.5	14359.42	1.5	0.63 ± 0.08	-2.06
6855.30	28068.79	1.5	13485.56	2.5	0.060 ± 0.00 0.060 ± 0.011	-2.77
6935.17	31784.16	1.5	17368.87	2.5	0.099 ± 0.019	-2.55
6980.90	29405.12	2.5	15084.26	3.5	0.43 ± 0.07	-1.73
7663.09	33180.92	2.5	20134.94	2.5	0.112 ± 0.029	-2.23
7757.91	31784.16	1.5	18897.64	1.5	0.34 ± 0.08	-1.91
7801.51	28068.79	1.5	15254.29	0.5	0.054 ± 0.001	-2.70
	_00000		±0=0 ±•=0	J. J	5.001 <u> </u>	

Table 3—Continued

$\lambda_{air} \ (ext{Å})$	$E_{upper} $ (cm ⁻¹)	J_{upp}	E_{lower} (cm^{-1})	J_{low}	A-value (10^6 s^{-1})	Log(gf)
7861.23 10900.77					0.17 ± 0.04 0.081 ± 0.019	-2.03 -2.24

arXiv:astro-ph/0611036v1 1 Nov 2006

Table 4. Atmospheric Model parameters for the Sun and 10 metal-poor, r-process rich stars.

	Sun	HD 74462	HD 115444	HD 122956	HD 165195	HD 175305	HD 186478	HD 221170	BD+17 3248	CS 22892-001	CS 31082-001
T_{eff} (K)	5780	4700	4650	4510	4235	5040	4600	4510	5200	4800	4825
log g	4.45	2.00	1.50	1.55	0.80	2.85	1.45	1.00	1.80	1.50	1.50
v_{micro}	0.85	1.90	2.10	1.60	2.30	2.00	2.00	1.80	1.90	1.95	1.90
$[\mathrm{Fe/H}]$	0.00	-1.51	-2.90	-1.97	-2.51	-1.63	-2.51	-2.19	-2.10	-3.12	-2.92
Ref.	1	2	3	2	2	2	2	4	5	6	7

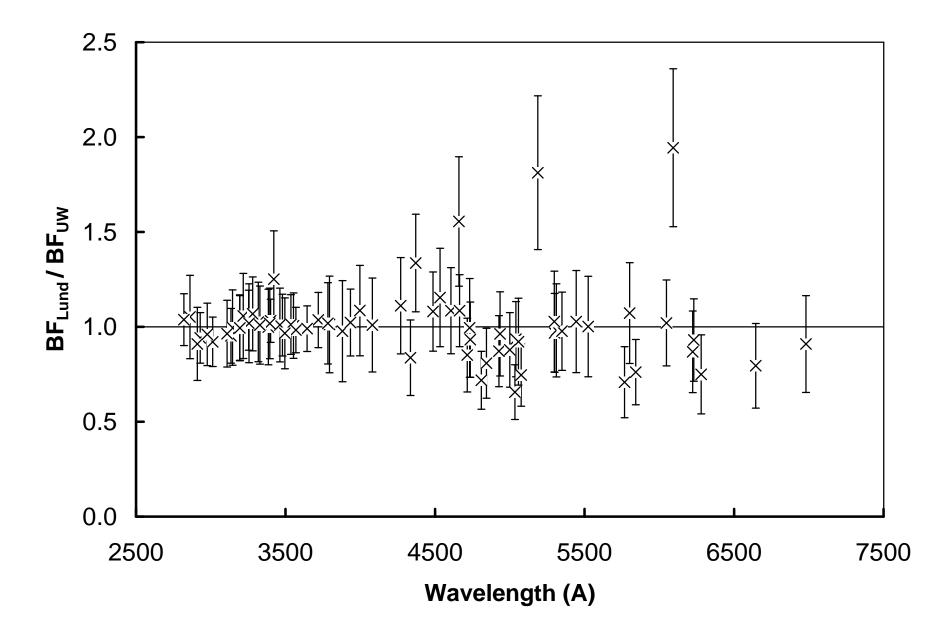
arXiv:astro-ph/0611036v1 1 Nov 2006

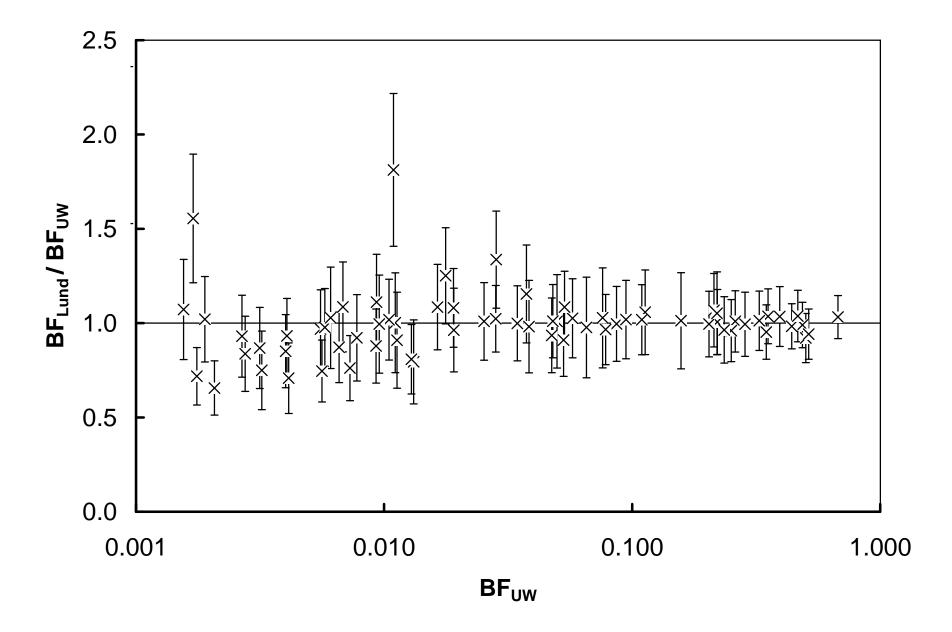
Table 5. Hafnium abundances, $\log(\varepsilon)$, from individual lines for the Sun and 10 metal-poor, r-process rich stars.

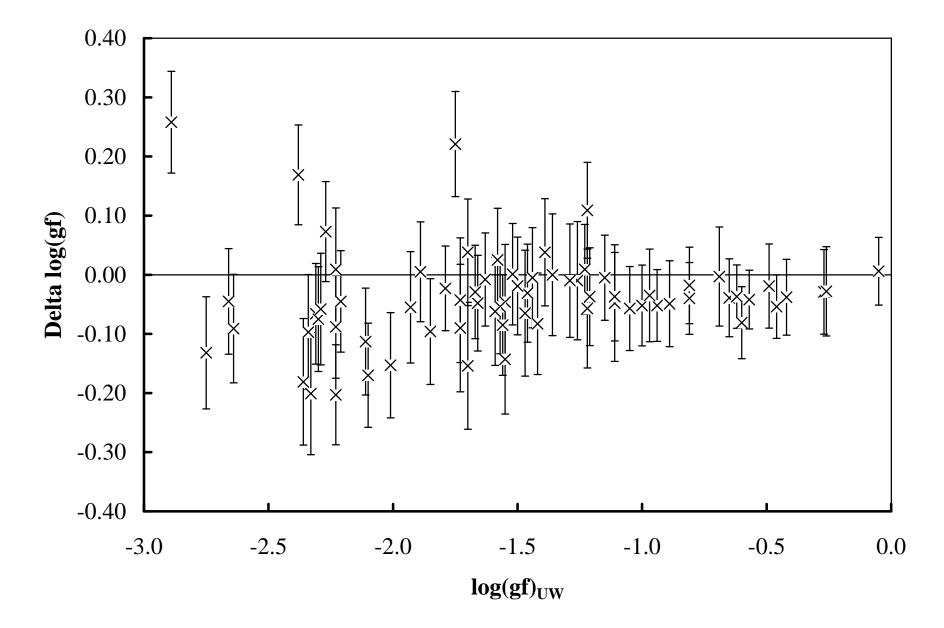
$\begin{matrix} \lambda \\ (\mathring{\rm A}) \end{matrix}$	χ (eV)	$\log(gf)$ Sur	HD 74462	HD 115444	HD 122956	HD 165195	HD 175305	HD 186478	HD 221170	BD+17 3248	CS 22892-001	CS 31082-001
3176.85	0.61	-0.80	-0.41		-0.74				-0.83	-0.60		
3193.53	0.38	-0.89	-0.43				-0.30	-1.33	-0.93	-0.55		-0.74
3389.83	0.45	-0.78 0.9	L						-0.88			-0.69
3399.79	0.00	-0.57									-0.90	-0.79
3479.29	0.38	-1.00							-0.68		-0.90	-0.69
3505.22	1.04	-0.14	-0.55	-1.52	-0.79				-0.88	-0.70	-0.90	-0.77
3535.55	0.61	-0.65							-0.83			
3561.66	0.00	-0.87 0.8	-0.58	-1.52	-0.84		-0.40		-0.98		-0.85	-0.67
3719.28	0.61	-0.81						-1.40	-0.88	-0.53	-0.85	-0.71
3793.38	0.38	-1.11									-0.93	-0.72
3918.09	0.45	-1.14 0.9	L	-1.52					-0.63	-0.45	-0.80	-0.69
4093.15	0.45	-1.15 0.8	6 -0.43	-1.47	-0.79	-1.36	-0.10	-1.38	-0.85	-0.58	-0.87	-0.69

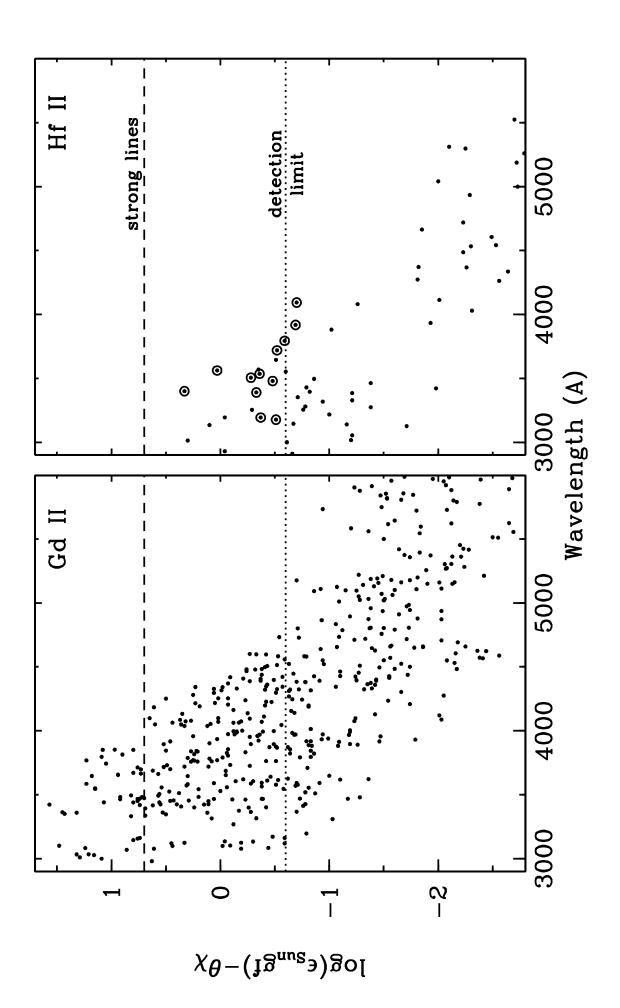
Table 6. Mean abundances, uncertainties, and number of lines used for the Sun and 10 metal-poor, r-process rich stars.

	Sun	HD 74462	HD 115444	HD 122956	HD 165195	HD 175305	HD 186478	HD 221170	BD+17 3248	CS 22892-001	3
Mean log $\varepsilon(Hf)$	0.88	-0.48	-1.51	-0.79	-1.36	-0.27	-1.37	-0.84	-0.57	-0.88	
±	0.02	0.04	0.01	0.02		0.09	0.02	0.03	0.03	0.01	
σ	0.03	0.08	0.03	0.04		0.15	0.04	0.11	0.08	0.04	
Number of Hf lines	4	5	4	4	1	3	3	10	6	8	
Mean log $\varepsilon(La)$	1.14	-0.28	-1.44	-0.61	-1.15	-0.07	-1.30	-0.73	-0.42	-0.84	
\pm	0.01	0.03	0.02	0.04	0.03	0.02	0.03	0.01	0.01	0.01	
σ	0.03	0.06	0.05	0.10	0.07	0.05	0.08	0.06	0.05	0.05	
Number of La lines	14	6	8	8	8	8	8	36	15	15	
Mean log $\varepsilon(Eu)$	0.52	-0.45	-1.64	-0.84	-1.30	-0.28	-1.48	-0.86	-0.67	-0.95	
土	0.01	0.04	0.01	0.03	0.03	0.02	0.02	0.02	0.02	0.02	
σ	0.04	0.09	0.03	0.07	0.07	0.06	0.04	0.07	0.05	0.05	
Number of Eu lines	14	4	6	5	5	6	6	16	9	8	
Mean log $\varepsilon(Hf/Eu)$	0.36	-0.03	0.13	0.05	-0.06	0.01	0.11	0.02	0.10	0.08	
Mean log $\varepsilon(\text{La/Eu})$	0.62	0.17	0.20	0.23	0.15	0.21	0.18	0.13	0.25	0.11	









Relative Intensity

